AIAA JOURNAL
Vol. 34, No. 10, October 1996

Detailed Mechanism of the Unsteady Combustion Around Hypersonic Projectiles

Akiko Matsuo*
Keio University, Yokohama, Kanagawa 223, Japan
and
Kozo Fujii†
Institute for Space and Astronautical Science, Sagamihara, Kanagawa 229, Japan

Flow features of an unsteady shock-induced combustion around projectiles are numerically studied using a finite difference method. The large-disturbance regime of the unsteady combustion, characterized by a low-frequency and high-amplitude oscillation, is investigated by a series of simulations considering an oxygen–hydrogen combustion mechanism under the same condition as the experiment. The time-evolving flowfield is obtained in the simulation, and the mechanism of the unsteady phenomenon is investigated. The mechanism on the stagnation streamline agrees with our previously proposed model using a simplified chemical reaction model. Several detailed features characterizing the large-disturbance regime of unsteady combustion are revealed in the computations, and an improved mechanism is proposed. The grid refinement study is carried out to confirm that the flow features obtained are grid independent and are not fictitious.

Nomenclature

M = projectile Mach number
P = pressure
T = temperature
t = time
V = projectile velocity
x = distance
τ = oscillation period
τ_x = induction time

Introduction

PERIODIC oscillations of the shock-induced combustion around a spherical projectile flying at hypervelocity into combustible gases were observed in a number of ballistic experiments[1–6] that were conducted during the 1960s and 1970s for possible application in the propulsion of missiles and aircraft. These periodic oscillations in the unsteady shock-induced combustion were characterized by two kinds of flow regimes: regular and large disturbance.[1] Alpert and Toong[1] investigated the periodic density variations in the burned gas observed in the nose region of the hypersonic blunt-body flows in the ballistic range experiments. Ruegg and Dorsey[2] investigated the problems of stabilizing combustion and detonation by the observation of a 20-mm spherical projectile fired into a stoichiometric mixture of hydrogen and air. They presented experimental results showing the regular and large-disturbance regimes. Figures 1a and 1b are the schlieren photographs of the experimental outputs obtained in their work. These photographs show typical flow features characterized by the large-disturbance regime. Changes of the projectile speed do not alter the combustion regime.

In the regular regime, the oscillation is very regular. A model of the regular regime of the unsteady combustion was proposed by McVey and Toong[3] using the x-t diagram on the stagnation streamline between the bow shock and the reaction front, based on the experimental observations and the one-dimensional wave interaction theory. In the large-disturbance regime, the oscillation is less regular but much more pronounced than that of the regular regime. Alpert and Toong[1] proposed a one-dimensional model to explain the periodicity of the large-disturbance regime. Their mechanism explains that one period of the large-disturbance regime is the long series of wave interactions of summing cycles of the four wave interactions of the regular regime, and each wave interaction depends on the strength of the reaction shock attenuated by the rarefaction wave.

The period of oscillation of the large-disturbance regime is several times longer than that of the regular regime. The oscillation period, τ, obtained from a number of experiments having different projectile velocities, projectile scale, projectile shape, degrees of dilution of the hydrogen and oxygen mixture, and initial pressures, was shown in Fig. 6 of Ref. 1. The period was normalized by the induction time τ_x in the nearly uniform region behind the normal segment of the bow shock. The results suggested that the range of the period of the large-disturbance regime is

$$3 < \tau/\tau_x < 12$$

The averaged period of the large-disturbance regime derived by the method of the least squares was

$$\tau/\tau_x \approx 5.23$$

Mechanism of the Unsteady Shock-Induced Combustion

Previous studies[7–12] reported that numerical simulations successfully reproduced the regular regime of the unsteady combustion. The proposed mechanism on the stagnation streamline between the bow

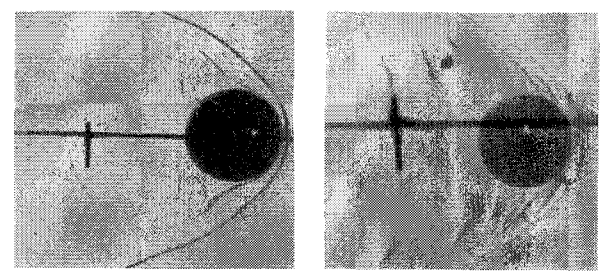

a) M = 4.3, V = 1758.7 m/s b) M = 4.8, V = 1963.2 m/s

Fig. 1 Experimental output by Ruegg and Dorsey[2] (P = 0.5 atm, T = 300 K).

Received June 6, 1995; presented as Paper 95-2565 at the AIAA/ASME/SAE/ASEE 31st Joint Propulsion Conference, San Diego, CA, July 10–12, 1995; revision received May 28, 1996; accepted for publication June 9, 1996.

*Research Associate, Department of Mechanical Engineering, 3-14-1, Hiyoshi. Member AIAA.
†Associate Professor, High-Speed Aerodynamics Division, 3-1-1, Yoshinodai. Associate Fellow AIAA.

shock and the projectile surface basically agreed with the mechanism proposed by McVey and Toong.[3] The regular regime of the unsteady combustion is characterized by the following statements. A compression wave created at the new reaction region interacts with the bow shock, and a contact discontinuity is generated. In general, the temperature on the right-hand side of the left-running contact discontinuity is higher than that on the left-hand side. Because the higher-temperature gas has the shorter induction time, new reaction occurs in front of the original reaction front. The generation cycle of the new-reaction region is periodically repeated in front of the projectile.

In the work of Matsuo and Fujii,[13] the mechanism of the large-disturbance regime was computationally studied using a simplified two-step chemical reaction model. A new model explaining the mechanism of the large-disturbance regime on the stagnation streamline proposed in that work is presented in Fig. 2. The proposed mechanism[13] is explained as follows: The step numbers referred to in the following text are indicated by the bracketed numbers in the left margin of Fig. 2. The beginning of the cycle is shown at step 1. The explosion at the reaction front is initiated, which is called an explosion in an explosion, and two strong shock waves are produced in both the right and the left directions. These compression waves are called reaction shocks because the compression waves in the large-disturbance regime are much stronger than those in the regular regime. The left-running reaction shock traveling into the burned gas is called a retonation. The right-running reaction shock moving into the unburned gas develops to a superdetonation. The superdetonation is accelerated by the reaction front, but the retonation moves at the speed of sound. At step 2, the detonation wave overtakes and penetrates the bow shock. Rarefaction waves and a contact discontinuity are generated there. After the penetration, the bow shock moves upstream and is accelerated, and the gas behind the bow shock wave is more compressed. At step 3, the bow shock starts moving back to the projectile surface and is decelerated, which makes the induction time exponentially longer, and the bow shock and the reaction front become separated. At step 4, the retonation reaches the body surface and reflects toward the bow shock. The reflected shock interacts with the bow shock at step 5, and the contact discontinuity is created. The temperature behind the contact discontinuity is higher than that before it, and the induction time becomes shorter. At step 6, the contact discontinuity reaches the original reaction front, and an explosion occurs. The cycle of the events is completed as

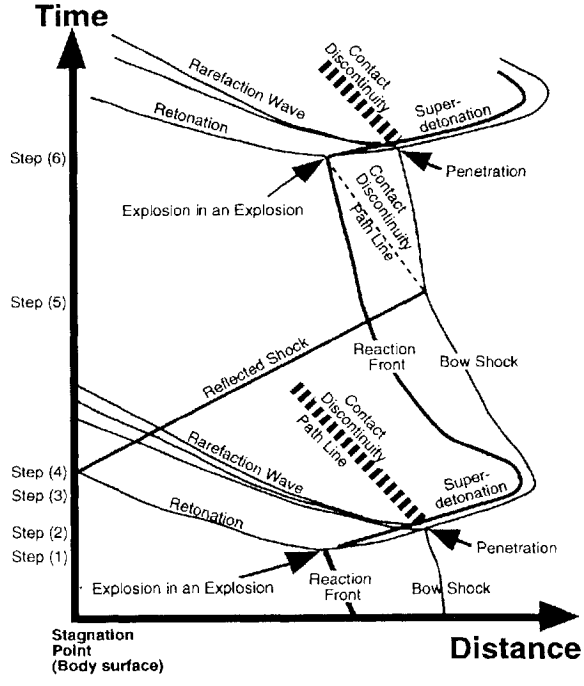

Fig. 2 An *x-t* diagram of the wave interaction model of the large-disturbance regime proposed by Matsuo and Fujii.[13]

another explosion in an explosion occurs. The similar mechanism is observed in the development of detonation from deflagration, which is called DDT for deflagration–detonation–transition.[14] However, in this mechanism of the large-disturbance regime, the reaction shock does not completely develop to the self-sustained detonation wave, and an explosion in an explosion is induced periodically.

The proposed mechanism was based on the simplified chemical reaction model. Direct comparison of the simulations using a more detailed oxygen–hydrogen reaction mechanism is necessary to show the validity of the proposed model. In the present study, a series of simulations using an oxygen–hydrogen reaction mechanism is carried out, and the detailed mechanism of the large-disturbance regime is investigated as well as the proposed model to be validated.

Mathematical Formulation

To verify the proposed model for the large-disturbance regime, the simulations using the Euler equations with the species conservation equations under the axisymmetric assumption are conducted. The equations are integrated explicitly, and the chemical reaction source term is treated in a linearly point-implicit manner. As a numerical scheme, Yee's non-MUSCL-type total variation diminishing (TVD) upwind explicit scheme[15] is used.

The governing system of equations for the inviscid flows and the axisymmetric geometry is

$$\frac{\partial \hat{Q}}{\partial \tau} + \frac{\partial \hat{E}}{\partial \xi} + \frac{\partial \hat{F}}{\partial \eta} = \hat{S} + \hat{H}$$

where $\hat{E}$ and $\hat{F}$ are the inviscid flux vectors in the ξ and η directions, respectively; $\hat{S}$ is the chemical reaction source vector; and $\hat{H}$ is the axisymmetric term.

Reaction Model

The oxygen–hydrogen combustion mechanism used in this study is the same as that of the work by Wilson.[16] This reaction set was developed for a supersonic combustion. It basically consists of 13 reacting species (H_2, O_2, H, O, OH, H_2O, HO_2, H_2O_2, N, NO, NO_2, HNO, and N_2) and 33 reactions and is a modification of Jachimowski's[17] combustion mechanism. The nitrogen reactions are not important at Mach numbers less than 5, and all nitrogen reactions are omitted, although N, NO, HNO would become important at higher Mach numbers. Therefore, only 8 species (H_2, O_2, H, O, OH, H_2O, HO_2, and H_2O_2) and 19 reactions, as cited in Table 1, are used, and the nitrogen molecule is included as an inert species. The thermochemical data used for the nine species are obtained from NASA thermochemical polynomials.[16]

Table 1 H_2–O_2 reaction mechanisms[a]

k	Reaction	A	n	E
1	$H_2 + O_2 = HO_2 + H$	1.00×10^{14}	0.0	56,000
2	$H + O_2 = OH + O$	2.60×10^{14}	0.0	16,800
3	$O + H_2 = OH + H$	1.80×10^{10}	1.0	8,900
4	$OH + H_2 = H + H_2O$	2.20×10^{13}	0.0	5,150
5	$OH + OH = O + H_2O$	6.30×10^{12}	0.0	1,090
6	$H + OH + M = H_2O + M$	2.20×10^{22}	−2.0	0
7	$H + H + M = H_2 + M$	6.40×10^{17}	−1.0	0
8	$H + O + M = OH + M$	6.00×10^{16}	−0.6	0
9	$H + O_2 + M = HO_2 + M$	2.10×10^{15}	0.0	−1,000
10	$O + O + M = O_2 + M$	6.00×10^{13}	0.0	−1,800
11	$HO_2 + H = OH + OH$	1.40×10^{14}	0.0	1,080
12	$HO_2 + H = H_2O + O$	1.00×10^{13}	0.0	1,080
13	$HO_2 + O = O_2 + OH$	1.50×10^{13}	0.0	950
14	$HO_2 + OH = H_2O + O_2$	8.00×10^{12}	0.0	0
15	$HO_2 + HO_2 = H_2O_2 + O_2$	2.00×10^{12}	0.0	0
16	$H + H_2O_2 = H_2 + HO_2$	1.40×10^{12}	0.0	3,600
17	$O + H_2O_2 = OH + HO_2$	1.40×10^{13}	0.0	6,400
18	$OH + H_2O_2 = H_2O + HO_2$	6.10×10^{12}	0.0	1,430
19	$H_2O_2 + M = OH + OH + M$	1.20×10^{17}	0.0	45,500

[a] $k_{f_k} = AT^{n_k} \exp(-E_k/RT)$; units are in seconds, moles, cubic centimeters, calories, and Kelvin. Third-body efficiencies relative to N_2: reaction 6, $H_2O = 6.0$; reaction 7, $H_2O = 6.0$, $H_2 = 2.0$; reaction 8, $H_2O = 5.0$; reaction 9, $H_2O = 16.0$, $H_2 = 2.0$; and reaction 19, $H_2O = 15.0$.

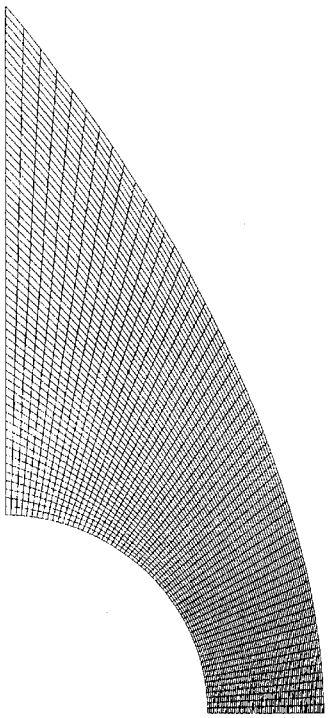

Fig. 3 Every 10th point of computed grid for case 1.

Computational Setup

Domain

In this study, the computational domain is limited to the region in front of the hemispherical nose of the blunt body, and the flow is assumed to be axisymmetric, based on the experimental observations. The number of grid points is 601 × 601, which are equally distributed in each direction. The flow computations are carried out first for the inert air, and the result is used as an initial condition for the hydrogen–air gas mixture. The grid distribution used in the present computations for case 1 (projectile speed 1758.7 m/s) is shown in Fig. 3.

Flow Configuration

The flow conditions of the experiments by Ruegg and Dorsey[2] in Figs. 1a and 1b are simulated. The conditions are as follows: gas mixture, $2H_2 + O_2 + 3.76\ N_2$; pressure, 0.5 atm; temperature, 300 K; projectile diameter, 20 mm; projectile speed, case 1, 1758.7 m/s ($M = 4.3$) in Fig. 1a, and case 2, 1963.2 m/s ($M = 4.8$) in Fig. 1b.

Initial Condition

To capture physical instabilities derived by the shock-induced combustion, initial disturbances introduced by the impulsive start of the computation should be avoided. Therefore, the following technique is used. The flowfield of the inert air is first solved under the same projectile velocity, gas temperature, and gas pressure as the hydrogen–air gas mixture. At the beginning of the reacting-flow computation, the converged flowfield of the inert air is used behind the bow shock wave, but the air in front of the bow shock is replaced by a combustible gas mixture. The exothermic reaction gradually starts in the combustible gas flows through the bow shock wave.

Results of Case 1

Histories on the Stagnation Streamline

An x-t diagram of the density contour distributions on the stagnation streamline is shown in Fig. 4. The horizontal axis denotes the distance from the stagnation point. The vertical axis denotes the physical time from the beginning of the reacting-flow computation. The left end of the horizontal axis corresponds to the projectile surface. The bow-shock location is indicated by the density jump at the far right, and the density change behind the bow shock indicates an onset of the exothermic reaction. Between the bow shock wave and the projectile surface, many wave interactions are observed. The location of the bow shock and the reaction front periodically

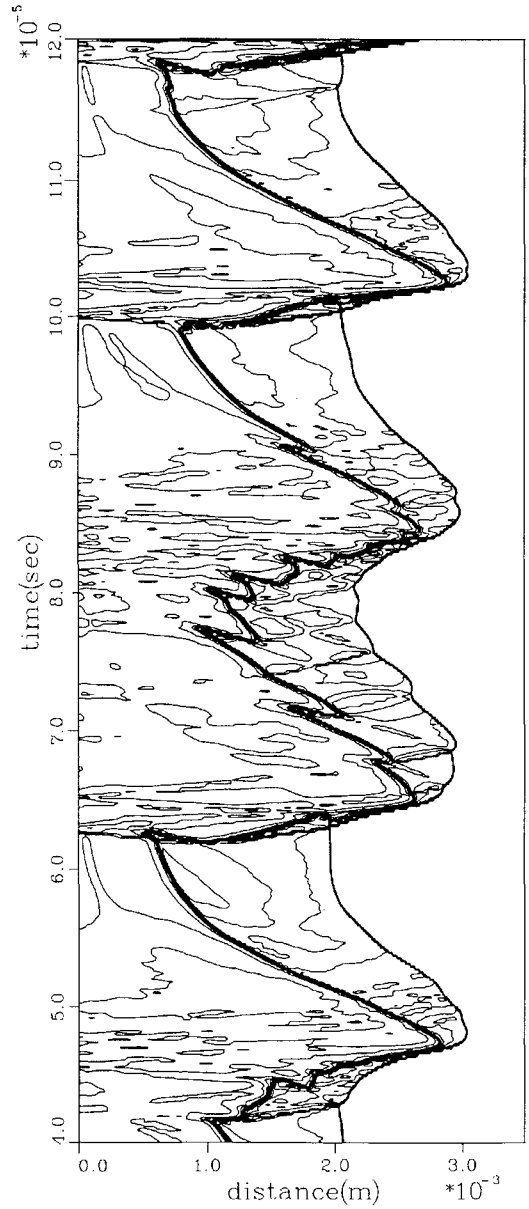

Fig. 4 History of the density contour distributions on the stagnation streamline for the projectile speed 1758.7 m/s: contour range min = 1.0, max = 4.15, and increment = 0.15 kg/m^3.

and synchronously moves right and left, and four cycles of the unsteady combustion are observed. The periodicity of the unsteadiness is clearly recognized in this x-t diagram, although the detailed flow structure changes cycle to cycle.

Figure 5 shows the histories of the shock standoff distance and the location of the reaction front on the stagnation streamline. The pressure at the shock front is also plotted. The pressure is normalized by the steady pressure level behind the normal segment of the bow shock wave. The time and the distance in Fig. 5 correspond to those in Fig. 4. As indicated in Fig. 5, two kinds of pressure spike, (a) and (b), are observed. Spike (a) has several small peaks, and the pressure level gradually increases with the small peaks. On the other hand, the pressure level of spike (b) suddenly increases and has only two sharp peaks. Although each pressure spike does not exactly show the same feature, the period of the pressure spikes is almost constant. The period of the oscillation obtained by an averaged time of four cycles is 18.5 μs. Because the induction time is 3.278 μs, the normalized period of the oscillations, τ/τ_x, is 5.65, which is within the range of the experimental observations. Here, the induction time was calculated by the zero-dimensional analysis,[13] which was carried out by the time integration of the species equations in the zero dimensioned space under the constant-volume mode (total density is constant) of the thermally perfect gas mixture. Figure 6 is a closeup view of

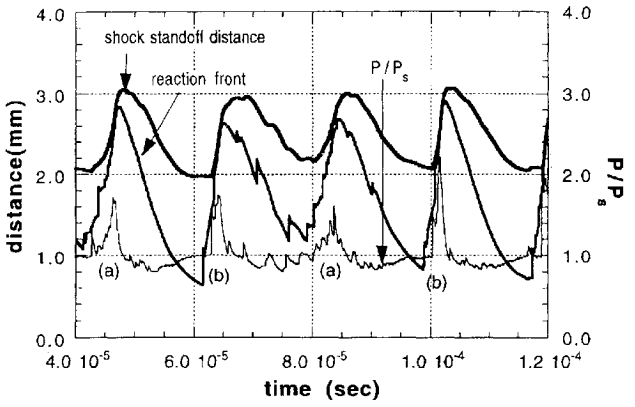

Fig. 5 Histories of the shock standoff distance and the location of the reaction front on the stagnation streamline for the projectile speed 1758.7 m/s. (P_s is the steady pressure level behind the normal segment of the bow shock.)

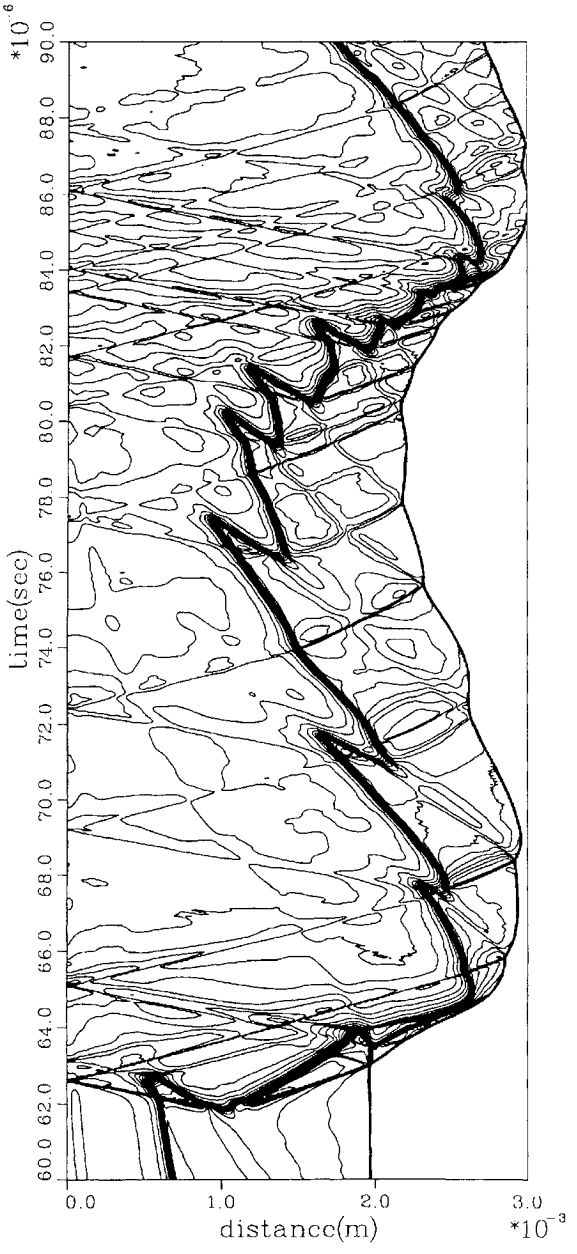

Fig. 6 Closeup view of the density contour distributions on the stagnation streamline between 60.0 and 90.0 μs in Fig. 4: contour range min = 1.0, max = 3.25, and increment = 0.075 kg/m^3.

the x-t diagram of the density contour distributions on the stagnation streamline from 60.0 to 90.0 μs of Fig. 4. The origins of pressure spikes (a) and (b) are shown in Fig. 6. These spikes are caused by the wave interactions around 80.0 and 62.0 μs, respectively.

As for pressure spike (a), new reaction regions induced along the contact discontinuities are intermittently created in the unburned gas region. The schematic picture of the wave interactions of spike (a) is shown in Fig. 7. Reaction shocks are released both rightward and leftward at each new reaction region. As the mechanism explained in Fig. 2, the bow shock is decelerated after the penetration. The new reaction regions are induced along the contact discontinuities at 67.0, 71.0, and 77.0 μs and are located gradually away from the bow shock. At 78.0 μs, the bow shock stops moving toward the projectile and starts moving upstream. From 79.0 μs, new reaction regions move closer to the bow shock. As explained in Fig. 2, the acceleration and deceleration change the bow-shock strength. The induction length changes accordingly, and the location of the onset of the new reaction moves away from or closer to the bow shock wave. The bow shock is pushed away from the projectile surface by the intermittent interactions in the cycle. In other words, the reaction shock is strengthened by the intermittent self-enforced explosions in the current cycle. According to the mechanism in Fig. 2, the reaction shock develops to a superdetonation, but the simulation result in Fig. 6 does not show the fully developed detonation. The mechanism generating new explosions of spike (a) is essentially the same as that in the regular regime. However, the reaction shocks generated in this mechanism are so strong that the shock strength of

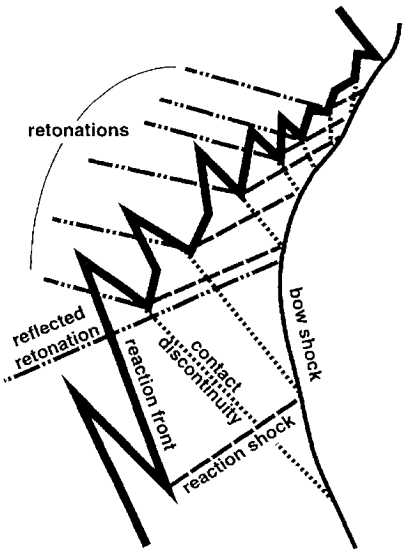

Fig. 7 Schematic of the submechanism (self-enforced explosion) of the large-disturbance regime for the projectile speed 1758.7 m/s.

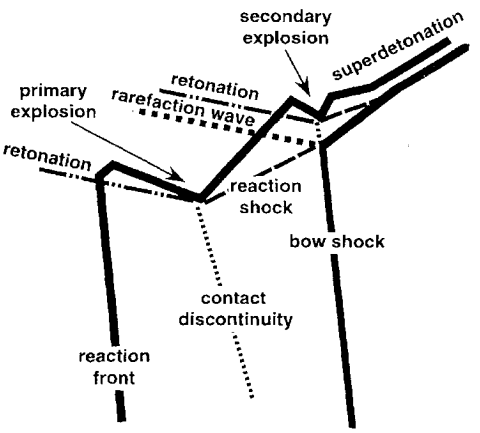

Fig. 8 Schematic showing the submechanism (secondary explosion) of the large-disturbance regime for the projectile speed 1758.7 m/s.

the bow shock is gradually strengthened, and finally, the mechanism shows the feature of the large-disturbance regime.

On the other hand, the feature of pressure spike (b) in Fig. 6 has a rather simple flow structure. The schematic of the wave interactions of spike (b) is shown in Fig. 8. A new explosion is induced in front of the original reaction front, and the rightward reaction shock and the retonation are created. The reaction shock compresses the unburned gas and, as a result, the reaction region expands in front of the projectile. However, the reaction shock is not strong enough to develop to a superdetonation. The reaction shock interacts and penetrates the bow shock at 63.0 μs. At the penetrating point of the reaction shock, a strong contact discontinuity and a rarefaction wave are generated. If the reaction shock developed to the full detonation wave, the pressure spike (b) in Fig. 5 should have one peak. However, the reaction shock is not a detonation wave, and a secondary explosion is induced along the contact discontinuity. Then, the secondary explosion occurs in front of the original reaction front, and the reaction shock and the retonation are created again. After the secondary explosion, the reaction shock is followed by the reaction front and becomes a superdetonation, and the retonation generated at the secondary explosion follows the rarefaction wave in the burned-gas region. The basic mechanism of the secondary explosion is the same as that of the self-enforced explosion. Therefore, the secondary explosion is considered as one feature of the self-enforced explosion.

The self-enforced explosion and the secondary explosion are recognized as the submechanism of the mechanism explained in Fig. 2 because the key factors, such as the explosion in the explosion, the penetration of the reaction shock, and the movement of the bow shock and the reaction front, also are observed in Figs. 4–6.

Flowfields Around the Projectile

The flowfields around the projectile should be examined for a better understanding of the flow pattern and the periodicity. Figure 9 (15 frames) shows the time-evolving profile of the density contour plots. The time interval between each frame is 2.0 μs. The time labeled in Fig. 9 corresponds to the time histories on the stagnation streamline shown in Figs. 4–6.

At 62.0 μs, a new reaction region is created in front of the projectile. This flowfield indicates the flow pattern of the secondary explosion on the stagnation streamline. At 64.0 μs, the burned-gas region expands ahead of the projectile, and the new explosion seems to occur near the bow shock. From 66.0 to 70.0 μs, the propagation of the burned-gas region induced by the secondary explosion are observed. The triple point, which is the merging point of the bow shock and the reaction front, moves along the bow shock, but the reaction front separates from the bow shock in front of the projectile. The pressure wave released at the primary explosion is overtaken by the reaction front moving with the triple point so that the propagating speed of the reaction front to the downstream must be supersonic. From 72.0 to 82.0 μs, new burned-gas regions are intermittently observed in front of the projectile. This is the flow pattern showing the self-enforced explosion on the stagnation streamline. At 84.0 μs, the burned-gas region eventually merges with the bow shock. From 84.0 to 88.0 μs, the triple point, which denotes the flow structure of the detonation wave front, moves along the bow shock, but the reaction front separates from the bow shock in front of the projectile. The flow pattern of each submechanism does not show a big difference in the global flowfield. Thus, the submechanism is considered to be a small feature of the mechanism of the large-disturbance regime, but it is imagined that these submechanisms cause less regular flow patterns in comparison with the mechanism of the regularbreak regime.

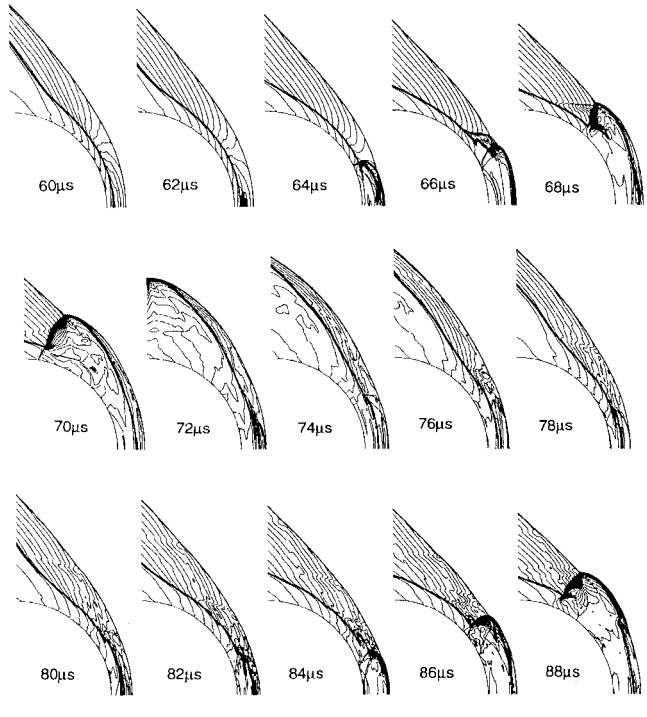

Fig. 9 Time evolution of the density contour plots between 60.0 and 88.0 μs or the projectile speed 1758.7 m/s: interval of the plots is 2.0 μs and contour range min = 0.1, max = 4.0, and increment = 0.1 kg/m^3.

The flow structure between the bow shock and the reaction front around the triple point is similar to the wave front of the detonation, showing the cellular structure. In general, the self-sustained detonation waves consist of transverse waves. The neighboring transverse waves collide, and the triple points of the detonation wave front write the pattern of the cellular structure. Here, the triple points in the present simulation move only downstream axisymmetrically along the bow shock wave, and no neighboring transverse waves collide.

Results of Case 2

Histories on the Stagnation Streamline

An x-t diagram of the density distributions on the stagnation streamline of case 2 (1963.2 m/s) is shown in Fig. 10. The bow-shock location is indicated by the rightmost density jump. The density decrease caused by the onset of the exothermic reaction is similar to that observed in Fig. 4. The location of the bow shock and the reaction front periodically and synchronously move right and left, and five cycles of the large-disturbance regime of the unsteady combustion are observed. The periodicity of the flow pattern is recognized.

Figure 11 shows the histories of the shock standoff distance, the reaction front location, and the normalized pressure level of the shock front. The time and the distance correspond to those in Fig. 10. The shock standoff distance gradually becomes longer during the computation, and the period of the pressure spikes also becomes longer. Each pressure spike has one strong peak, and the peak pressure level is much higher than that in Fig. 5, which indicates that the explosion in this case is much stronger than that in case 1. It is expected that the reaction shock may be fully developed detonation waves and will penetrate the bow shock wave. Eventually, the shock standoff distance and the period of the pressure spikes settle down, and the period is about 10.0 μs. In comparison with the case 1, the period of the pressure spikes is about half. However, the normalized period τ/τ_s of oscillations is 12.4 because the induction time is 0.805 μs. This is within the range of the experimental observations. As observed in the history of the pressure level, high-frequency and low-amplitude pressure fluctuations are observed before each pressure spike. Figure 10 shows the origins of such fluctuations. The fluctuations are caused by the wave interactions between the bow shock and the reaction shock or the retonation reflected on the projectile surface, which is considered as one of the features of the self-enforced explosion submechanism in the case 1.

Figure 12 is a closeup of the x-t diagram of the density-contour distributions on the stagnation streamline from 12.0 to 15.0 μs. This x-t diagram shows the typical wave interaction of the large-disturbance regime, which is explained in Fig. 2. The origin of the pressure spike and the penetration of the superdetonation are clearly observed. The explosion is induced at the reaction front, which is called the explosion in the explosion, and the strong reaction shock and the retonation are created. The reaction shock is immediately followed by the reaction front, so that the reaction shock is a superdetonation wave. At the penetrating point of the superdetonation,

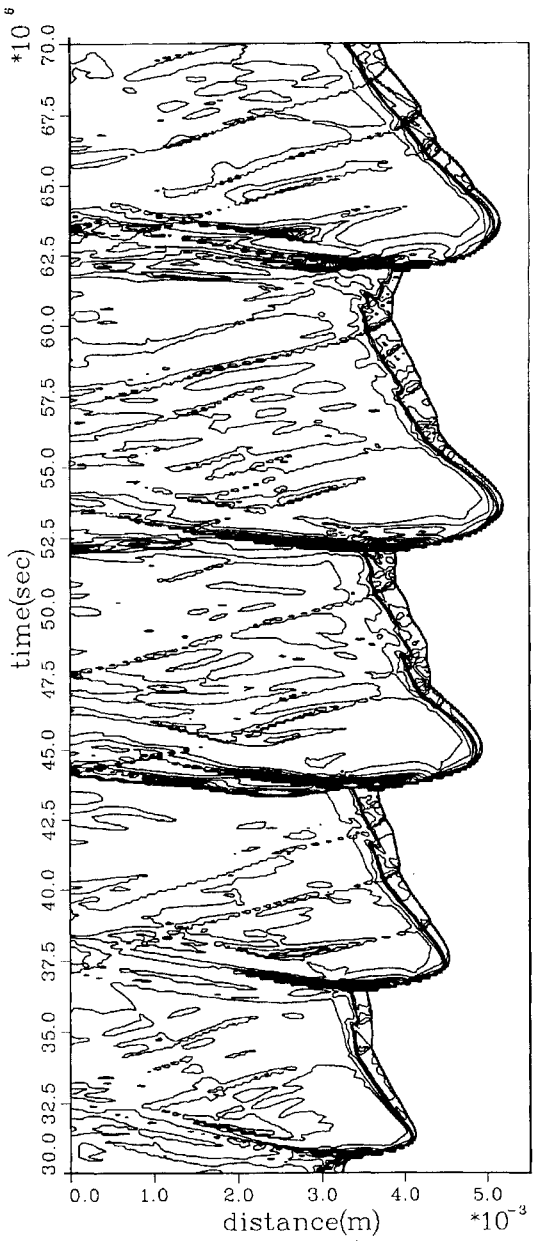

Fig. 10 History of the density-contour distributions on the stagnation streamline for the projectile speed 1963.2 m/s: contour range min = 1.0, max = 11.0, and increment = 0.25 kg/m^3.

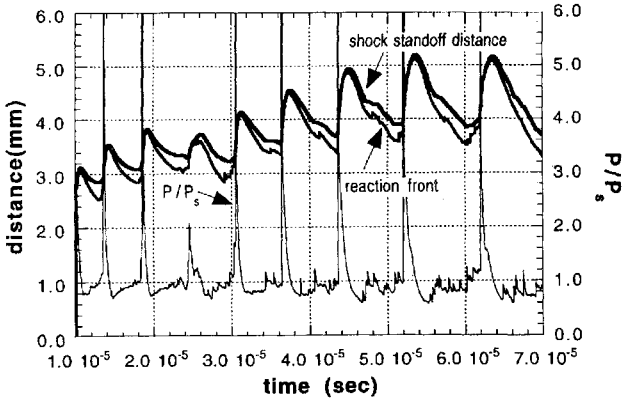

Fig. 11 Histories of the shock standoff distance, the location of the reaction front, and the pressure at the shock front on the stagnation streamline for the projectile speed 1963.2 m/s. (P_s is the steady pressure level behind the normal segment of the bow shock.)

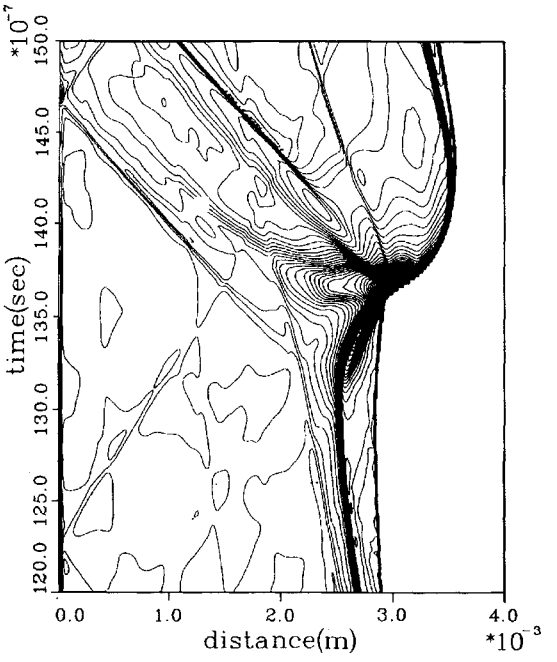

Fig. 12 Closeup of the density-contour distributions on the stagnation streamline between 12.0 and 15.0 μs: contour range min = 0.4, max = 5.55, and increment = 0.075 kg/m^3.

the rarefaction wave and the strong contact discontinuity are generated. This mechanism exactly agrees with the mechanism that we proposed in a previous study[13] (see Fig. 2). However, the retonation is observed between the rarefaction wave and the contact discontinuity and seems to be generated at the penetrating point. The reason supposedly is that the detonation wave is slightly decoupled at the penetrating point, so that the secondary explosion is induced after the penetration along the contact discontinuity.

Figure 13 is a closeup of the x-t diagram of the density-contour distributions on the stagnation streamline from 34.0 to 39.0 μs. This x-t diagram shows a typical example of the wave interactions after 20.0 μs. The flowfield is different from the mechanism of the large-disturbance regime explained in the preceding sections because the explosion occurs at the bow shock instead of on the reaction front or in the unburned-gas region. The explosion is considered to be a triple point that is induced off axis and comes to the stagnation streamline along the bow shock. The shock at 37.0 μs also is considered to occur somewhere off axis. The origin of the high-frequency and low-amplitude fluctuations in Fig. 11 is observed as the wave interactions between the bow shock and the reaction front.

Flowfield Around the Projectile

Figure 14 is the density-contour plot around the projectile at 40.0 μs. The five cycles of the triple point, which is the merging point of the bow shock and the reaction front, are regularly located along the bow shock. The periodicity of the unsteady shock-induced combustion is recognized in the flowfield. The flow pattern of the triple point is similar to the detonation wave front, and the triple points in this simulation result move only downstream along the bow shock, like those in Fig. 9.

Figure 15 (seven frames) shows a closeup of the time-evolving profile in front of the projectile (0.0–22.5 angle) of the density contour plots. The interval between each plot is 0.5 μs. The times labeled in Fig. 15 correspond to the times of the x-t diagram on the stagnation streamline in Fig. 12. The triple point appears at 12.0 μs, and the movement of the triple point is clearly observed from 12.0 to 13.0 μs. At 13.5.0 μs, a new burned-gas region occurs in front of the projectile. From 13.5 to 14.5 μs, the burned-gas region expands ahead of the projectile. This flow pattern agrees well with that indicated in Fig. 16 of Ref. 13. At 14.0 μs, the burned-gas region merges into the bow shock, and the merging point starts moving downstream along the bow shock.

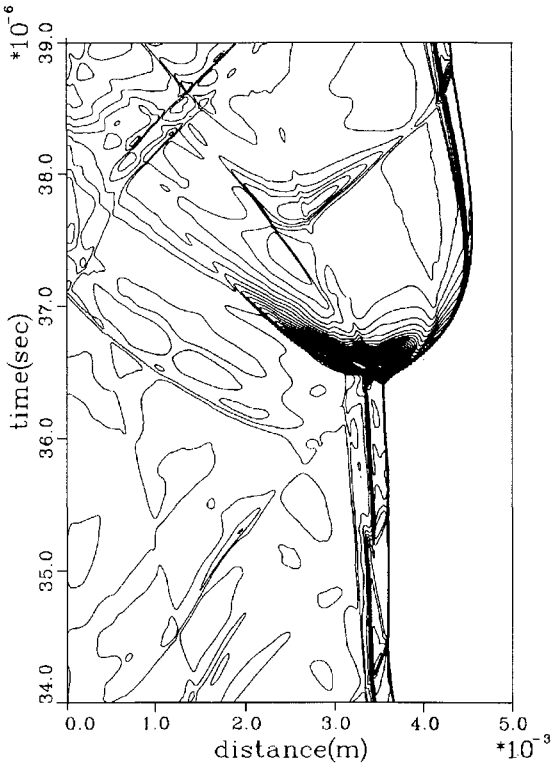

Fig. 13 Closeup of the density-contour distributions on the stagnation streamline between 34.0–39.0 μs in Fig. 10: contour range min = 0.6, max = 12.0, and increment = 0.15 kg/m^3.

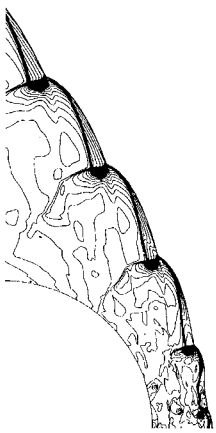

Fig. 14 Density contour plots at 40.0 μs for the projectile speed 1963.2 m/s: contour range min = 0.4, max = 4.3, and increment = 0.1 kg/m^3.

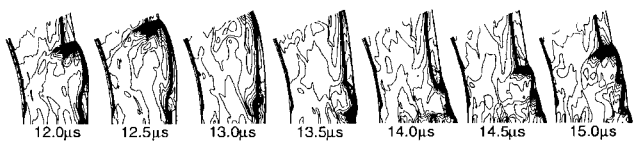

Fig. 15 Time evolution of the density-contour plots between 12.0–15.0 μs for the projectile speed 1963.2 m/s: interval of the plots is 0.5 μs and contour range min = 0.4, max = 6.0, and increment = 0.075 kg/m^3.

Next, the flowfields of Fig. 13 are shown in Fig. 16. Figure 16 (12 frames) shows a closeup of the time-evolving profile of the density-contour plots as in Fig. 15. The triple point moves along the bow shock from 33.0 to 34.0 μs. Here, the strongly curved reaction front stays around the stagnation streamline. Behind the curved reaction front a vortex is observed that is generated by the strongly curved shock structure after the penetration. An explosion in an explosion occurs in the unburned-gas region beside the stagnation streamline at 35.0 μs. From 35.5 to 36.5 μs, a spherical explosion wave consisting of the detonation and the retonation is clearly observed.

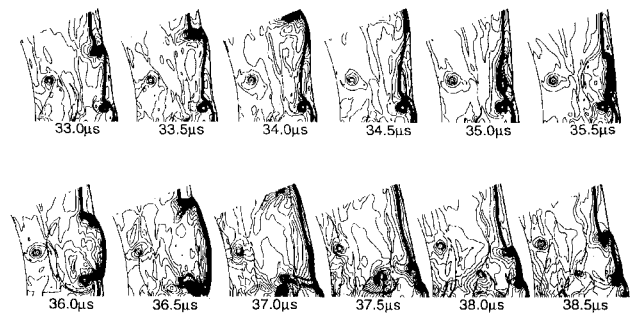

Fig. 16 Time evolution of the density-contour plots between 33.0–38.5 μs for the projectile speed 1963.2 m/s: interval of the plots is 0.5 μs and contour range min = 0.4, max = 6.0, and increment = 0.075 kg/m^3.

The triple points propagate in both directions on the bow shock as the transverse wave. Here, the explosion initiating the unsteady mechanism is not axisymmetric because it occurs somewhat away from the stagnation streamline. The interval of each cycle in the flowfield is much shorter than that of case 1, which corresponds to the two-dimensional detonation wave front supported by the piston. Furthermore, the particle path on the stagnation streamline does not arrive directly at the projectile surface because of the vortex behind the reaction front. Therefore, the exact simulations under the axisymmetric assumption would be difficult for the high-frequency mode of the large-disturbance regime of the unsteady combustion, but the characteristics of the mechanism are reproduced and are clearly recognized.

Characteristics of the Large-Disturbance Regime

The simulation results essentially agreed with the mechanism to explain the large-disturbance regime of the unsteady combustion explained in Fig. 2. The mechanism in Fig. 2 shows a typical one. A superdetonation induced by an explosion in an explosion at the original reaction front penetrates the bow shock and finally separates into the bow shock and the reaction front. The importance of the explosion in the explosion and the superdetonation that was pointed out in the work of Matsuo and Fujii[13] was confirmed by the present study. The simulation result of case 2 agreed well with the typical mechanism.

Furthermore, the detailed features of the large-disturbance regime of the unsteady combustion on the stagnation streamline were clarified in the observation of the simulation results, and submechanisms as the self-enforced explosion and the secondary explosion were revealed, based on the simulation results of the case 1. The steady shock strength of the bow shock in case 1 is weaker than that in case 2, and the compression of the bow shock is required much more in case 1 to induce the fully developed detonation wave than in case 2. Thus, an additional mechanism for the compression of the bow shock is necessary. Therefore, such submechanisms are considered as one feature of the mechanism of the large-disturbance regime and are involved in the basic mechanism explained in Fig. 2. The submechanisms are summarized below.

Self-Enforced Explosion: A new reaction region occurs in front of the original reaction front, and a generated reaction shock interacts with the bow shock wave. The shock strength of the reaction shock is so strong that a new explosion occurs away from the original reaction front along the contact discontinuity. The new reaction shock interacts again. Because the bow shock wave is pushed away from the projectile surface by the intermittent interactions, the bow shock is accelerated, and the reaction front moves closer to the bow shock. Eventually, the reaction front separates from the bow shock because of the deceleration of the bow shock.

Secondary Explosion: A primary explosion occurs, and the strong reaction shock and the retonation are generated. The reaction shock directly penetrates the bow shock, though it is not followed by the reaction front. At the penetrating point, the strong contact discontinuity and the rarefaction wave are generated. A new explosion, called a secondary explosion, is induced along the contact discontinuity, and a superdetonation is created. Eventually, the reaction front separates from the bow shock, and the new cycle will be induced.

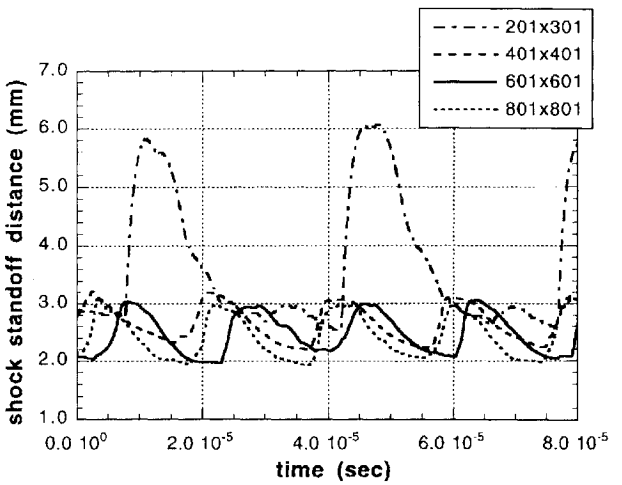

Fig. 17 Histories of the shock standoff distance on the stagnation streamline for the grid refinement study.

Basically, the mechanism of the secondary explosion is included in that of the self-enforced explosion.

The flow pattern characterized by the transverse wave moving along the bow shock, which consists of the triple point of the bow shock and the reaction front, is also a typical feature of the large-disturbance regime of the unsteady combustion. The basic configuration of the flow pattern is similar to the wave front of the self-sustained detonation, but the large-disturbance regime of the unsteady combustion is sustained by the projectile body.

Grid Refinement Study

The grid refinement study is carried out to confirm that the flow features obtained are independent of the grid resolution. Figures 5 and 11 show the simulation results of the grid points 601×601. The sequence of the grid distributions, 201×301, 401×401, 601×601, and 801×801, is used for the grid refinement study in the case of the projectile velocity 1758.7 m/s. Figure 17 shows the histories of the shock standoff distance of each case. The horizontal axis denotes the physical time of the periodic unsteadiness after the initial numerical disturbance. As shown in Fig. 17, only the case of the grid points 201×301 shows very different features. The period is twice that of the others and the shock location changes very much. All other cases show the same trend. Therefore, the simulation result of the grid points 601×601 discussed in this study is essentially independent of the grid distribution. The mechanism of the wave interaction on the stagnation streamline of the grid points 201×301 is basically the same as the others, but the explosive intensity is changed by the lack of the grid resolution. In the case of the projectile velocity 1963.2 m/s, the different features are not observed in the results of the finer and coarser grid distribution, so that the simulation result in this study is independent of the grid resolution.

Conclusions

The large-disturbance regime of the unsteady combustion around the projectile was reproduced. Computations considering a detailed oxygen–hydrogen combustion mechanism under the same conditions as the experiment were carried out, and the time-evolving flowfields were obtained in the simulations. The mechanism on the stagnation streamline agrees with the previously proposed mechanism using the two-step reaction model. Two of the submechanisms for the large-disturbance regime were newly suggested in the present work. One is self-enforced explosion, in which the reaction shocks are strengthened by the intermittent explosion, and the other is secondary explosion, in which the primary strong reaction shock penetrates the bow shock, and the secondary explosion that develops to the superdetonation is induced along the contact discontinuity. It is clarified that the strength of the reaction shock is a key factor to determine the mechanism of the large-disturbance regime, and the acceleration and deceleration of the bow shock, which is pushed away by the reaction shock, is the key mechanism for the large-disturbance regime. The grid refinement study was carried out to confirm that the flow features obtained are grid independent and are not fictitious.

References

[1]Alpert, R. L., and Toong, T. Y., "Periodicity in Exothermic Hypersonic Flow About Blunt Projectiles," *Astronautica Acta*, Vol. 17, Nos. 4, 5, 1972, pp. 539–560.

[2]Ruegg, F. W., and Dorsey, W., "A Missile Technique for the Study of Detonation Wave," *Journal of Research of the National Bureau of Standards, Section C: Engineering and Instrumentation*, Vol. 66, No. 1, 1962, pp. 51–58.

[3]McVey, J. B., and Toong, T. Y., "Mechanism of Instabilities of Exothermic Hypersonic Blunt-Body Flow," *Combustion Science and Technology*, Vol. 3, No. 2, 1971, pp. 63–76.

[4]Lehr, H. F., "Experiments on Shock-Induced Combustion," *Astronautica Acta*, Vol. 17, Nos. 4, 5, 1972, pp. 589–597.

[5]Chernyi, G. G., "Supersonic Flow Past Bodies with Formation of Detonation and Combustion Fronts," *Astronautica Acta*, Vol. 13, Nos. 5, 6, 1968, pp. 467–480.

[6]Behrens, H., Struth, W., and Wecken, F., "Studies of Hypervelocity Firings into Mixtures of Hydrogen with Air or with Oxygen," *10th Symposium (International) on Combustion*, Combustion Inst., Pittsburgh, PA, 1965, pp. 245–252.

[7]Matsuo, A., and Fujiwara, T., "Numerical Investigation of Oscillatory Instability Mechanism in Shock-Induced Combustion Around an Axisymmetric Blunt Body," *AIAA Journal*, Vol. 31, No. 10, 1993, pp. 1835–1841.

[8]Matsuo, A., Fujiwara, T., and Fujii, K., "Flow Features of Shock-Induced Combustion Around Projectile Traveling at Hypervelocities," *AIAA Journal*, Vol. 33, No. 6, 1995, pp. 1056–1063.

[9]Yungster, S., and Radhakrishnan, K., "A Fully Implicit Time Accurate Method for Hypersonic Combustion: Application to Shock-Induced Combustion Instability," AIAA Paper 94-2965, July 1994.

[10]Wilson, G. J., and Sussman, M. A., "Computation of Unsteady Shock-Induced Combustion Using Logarithmic Species Conservation Equations," *AIAA Journal*, Vol. 31, No. 2, 1993, pp. 294–301.

[11]Ahuja, J. K., Tiwari, S. N., and Singh, D. J., "Investigation of Hypersonic Shock-Induced Combustion in Hydrogen-Air System," AIAA Paper 92-0339, Jan. 1992.

[12]Ahuja, J. K., and Tiwari, S. N., "Numerical Simulation of Shock-Induced Combusting in a Superdetonative Hydrogen-Air System," AIAA Paper 93-0242, Jan. 1993.

[13]Matsuo, A., and Fujii, K., "Computational Study of Large-Disturbance Oscillations in Unsteady Supersonic Combustion Around Projectiles," *AIAA Journal*, Vol. 33, No. 10, 1995, pp. 1828–1835.

[14]Urtiew, P. A., and Oppenheim, A. K., "Experimental Observation of the Transition to Detonation in an Explosive Gas," *Proceeding of the Royal Society of London, Series A: Mathematical and Physical Sciences*, Vol. 295, 1966, pp. 13–28.

[15]Yee, H. C., "Upwind and Symmetric Shock Capturing Schemes," NASA TM 89464, 1987.

[16]Wilson, G. J., "Computation of Steady and Unsteady Shock-Induced Combustion over Hypervelocity Blunt Bodies," Ph.D. Thesis, Dept. of Aeronautics and Astronautics, Stanford Univ., Stanford, CA, 1991.

[17]Jachimowski, C. J., "An Analytical Study of the Hydrogen-Air Reaction Mechanism with Application of Scramjet Combustion," NASA TP-2791, Feb. 1988.